Electrochimica Acta 354 (2020) 136748

Contents lists available at ScienceDirect

Electrochimica Acta

journal homepage: www.elsevier.com/locate/electacta

Corrosion and metal release investigations of selective laser melted 316L stainless steel in a synthetic physiological fluid containing proteins and in diluted hydrochloric acid

Masoud Atapour[a,b], Xuying Wang[a], Kim Färnlund[c], Inger Odnevall Wallinder[a], Yolanda Hedberg[a,*]

[a] KTH Royal Institute of Technology, School of Engineering Sciences in Chemistry, Biotechnology and Health, Department of Chemistry, Division of Surface and Corrosion Science, SE-10044 Stockholm, Sweden
[b] Department of Materials Engineering, Isfahan University of Technology, Isfahan 84156-83111, Iran
[c] AMEXCI AB, Gammelbackavägen 2, 69151 Karlskoga, Sweden

ARTICLE INFO

Article history:
Received 11 May 2020
Revised 22 June 2020
Accepted 7 July 2020
Available online 11 July 2020

Keywords:
Metal release
Corrosion
Stainless steel
Microstructure
Laser powder bed fusion

ABSTRACT

The corrosion and metal release characteristics of additively manufactured stainless steels are key factors for their applicability in biomedical applications. The effect of building direction on the microstructure, corrosion behavior and metal release of selective laser melted (SLM) AISI 316L stainless steel were therefore investigated in a protein-rich synthetic body fluid (PBS+BSA, pH 7.3) and in diluted hydrochloric acid (HCl, pH 1.5). A multi-analytical approach was applied to characterize SLM 316L surfaces printed in different building directions (denoted XY and XZ) and a post heat treated SLM surface (XZ-HT) compared with wrought surfaces. All SLM specimens revealed an austenitic microstructure without any amounts of δ-ferrite and without large-angled grain boundaries in contrast to the wrought 316L surface. The building direction strongly affected the grain size distribution due to the temperature gradients in the melt pools. The SLM 316L specimens released initially slightly less Fe, Cr and Ni compared with the wrought 316L specimen. Slightly less metal was released from the heat treated SLM specimen (XZ-HT) specimen compared to the other SLM specimens. Relatively high amounts of released Cr were observed in PBS+BSA, most probably attributed to protein-bound Cr, whereas substantially more Ni was released in HCl compared to PBS+BSA due to pitting corrosion and a reduced surface oxide thickness. The surface oxide composition of as-printed SLM specimens was strongly dependent on the building direction and the post heat treatment, whereas no differences were observed after abrasion either among the SLM specimens or compared with the wrought 316L specimen. Cr became in all cases enriched within the outermost surface oxide in PBS+BSA and strongly enriched in the HCl solution, coupled to a strongly reduced amount of released metals with time. The heat treated SLM specimen (XZ-HT) gained a superior charge transfer resistance, the lowest passive current density, and the highest OCP value among all specimens. In HCl, the SLM specimens showed a lower pitting susceptibility compared to the wrought specimens. No pitting was observed in PBS+BSA. No differences in corrosion or metal release characteristics were observed related to the building direction of abraded SLM specimens.

1. Introduction

The demand for high-performance implantable biomaterials has grown dramatically in the last decades, driven e.g. by an increasing middle age among the population, increased numbers of road accidents, increased incidence of chronic diseases and increased living standards [1,2]. By 2024, the global market of bioimplants is expected to reach a value of around 136.3 billion US$ [3]. At present, the greatest challenges of metallic biomaterials are the need for improved bio-functionality and the reduction of relatively high manufacturing costs [4]. Additive manufacturing (AM), of which one common method is selective laser melting (SLM), is currently exhibiting the fastest growth and innovation to overcome

* Corresponding author at: KTH Royal Institute of Technology, School of Engineering Sciences in Chemistry, Biotechnology and Health, Department of Chemistry, Division of Surface and Corrosion Science, SE-10044 Stockholm, Sweden.
E-mail addresses: m.atapour@cc.iut.ac.ir (M. Atapour), yolanda@kth.se (Y. Hedberg).

https://doi.org/10.1016/j.electacta.2020.136748

Table 1
Nominal bulk composition (wt%) of the virgin 316L powder used for SLM printing and of wrought 316L SS.

316L	Fe	Cr	Mn	Ni	Cu	Mo	N	C	S	Si	P
Virgin powder	Bal.	17.2	1.49	13.8	<0.005	2.92	0.08	0.009	<0.005	0.25	<0.01
Wrought	Bal.	16.9	1.3	10.1	0.48	2.0	0.05	0.017	0.0006	0.50	0.029

such challenges [5,6]. SLM, which is sub-classified as laser powder bed fusion (LPBF) emerges as an advanced manufacturing technology, offering high dimensional accuracy and flexible fabrication [7]. The integration of an implant in the body is associated with an evident risk of corrosion and metal release, processes that may lead to undesirable health problems, caused by (geno)toxic or allergenic properties of released metal species [8,9]. Rapid corrosion of implants can result in their premature failure and/or the deterioration of their mechanical properties [10]. Hence, it is vital to investigate the corrosion behavior of SLM biomedical alloys. Several studies have investigated the microstructure and mechanical properties of SLM materials, though studies on their corrosion behavior are still scarce [11,12]. A recent review [13] focused on the effects of AM parameters on the corrosion behavior of different AM alloys. The alloy microstructure, which depends on the laser power and the laser scan speed that dictate the thermal cycling and growth rate of the material during SLM processing, has been shown to strongly influence the corrosion behavior of SLM materials [14]. Another review [15] concludes that research on underlying reasons for the superior corrosion resistance of AM steels is still in its early stages and needs further exploration. Porosity has been shown to result in an enhanced formation of metastable pits and to reduce the repassivation potential of SLM 316L [13,14]. At the same time, limited formation of inclusions and of a more compact and protective surface oxide were observed for SLM stainless steels compared to their wrought counterparts [16–19]. Another study reports a higher corrosion susceptibility of SLM 316L compared to wrought 316L in 0.1 M HCl [20].

The total amount of metals released from biomedical implant materials in-vivo, including wear particles, metal ions, and metal species bound to ligands and proteins, depends on a combination of different chemical and physical processes. In protein-rich environments, adsorption-controlled complexation- or ligand-induced metal release mechanisms can take place in addition to, or in synergy with, other mechanisms such as metal oxidation [21–23]. The kind of protein(s) and concentration, temperature, as well as solution pH and composition are some important factors that have been shown to influence the metal release process from stainless steels in protein-containing solutions. To the best of our knowledge, metal release and corrosion of SLM 316L alloys in the presence of proteins have not yet been systematically investigated.

The objective of this work was to investigate the effect of post heat treatment and building direction of the SLM process on the microstructure, corrosion behavior and metal release of 316L stainless steel in a protein-rich synthetic body fluid and in diluted hydrochloric acid, simulating an environment at risk for promoting pitting or crevice corrosion of stainless steels.

2. Materials and methods

2.1. Sample fabrication and characterization

Micrometer-sized AISI 316L stainless steel (SS) powders (sphericity~1) were used during the SLM process by Amexci AB, Sweden. A traditionally wrought 316L sheet coupon, 2 mm in thickness, was evaluated as reference, Table 1. SLM specimens sized 15 × 15 × 1 mm were fabricated using optimized industrial parameters for fully-dense specimens (porosity < 0.08%). Two categories of SLM specimens were fabricated and investigated in this study, with the major surface parallel to the building platform (denoted SLM-XZ) and perpendicularly to it (SLM-XY) as illustrated in Fig. 1. Heat treated specimens were prepared from another set of SLM-XZ specimens, denoted XZ-HT. For this purpose, the temperature was gradually raised to 900 °C during 6 h and then kept at this temperature for 1.5 h in argon atmosphere before furnace-cooled. This post heat treatment was carried out in order to relieve inner stresses [24].

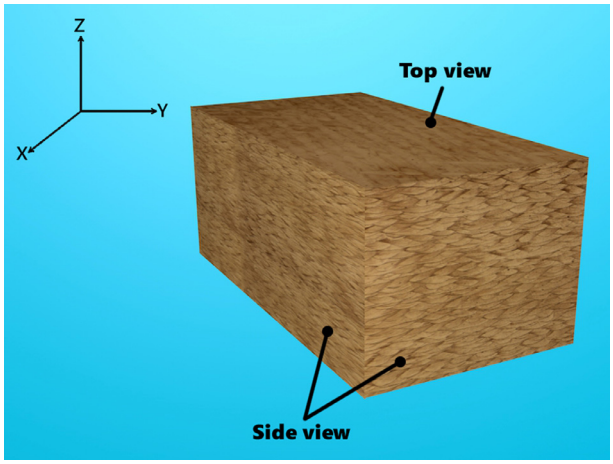

Fig. 1. Schematic view of the specimens fabricated by SLM constructed based on optical images of the microstructures observed after polishing and electro-etching (6 V for 20–30 s at room temperature) in 10 vol% oxalic acid.

2.2. Microstructure examinations

To examine the microstructure of the different materials, the specimens were ground and polished in steps down to 0.25 μm (diamond paste), chemically etched for 20 s in 10 mL nitric acid, 15 mL hydrochloric acid, 10 mL acetic acid, and two drops of glycerin, and ultrasonically cleaned in ethanol. Optical microscopic observations [Leica DM2770M light optical microscope (LOM) with a Leica DFC295 camera] were carried out on all corroded specimens. Scanning electron microscopy (tabletop Hitachi TM-1000) was also used.

Each specimen was prior to the electron backscattered diffraction (EBSD) investigations wet ground, polished with diamond paste to 0.25 µm, and subsequently polished with an active oxide suspension (OP-S, Struers, Sweden) and water for 15 h. A field emission gun scanning electron microscopy [FEG-SEM, 15 kV, 10 nA, aperture of 120 µm, Zeiss Sigma 300 VP (Gemini column) with Channel 5 software from HKL Technology and a Nordlys F+ EBSD camera] was used, along with energy x-ray dispersive spectroscopy (EDS) [Oxford Instruments, 80 mm^2 X-MaxN Silicon Drift Detector (SDD)].

Phase identification was performed using X-ray diffraction (XRD, Phillips, Netherlands) equipped with a CuKα radiation source (λ = 0.154 nm, 40 kV, 40 mA) scanning from 20 to 80° (2Θ).

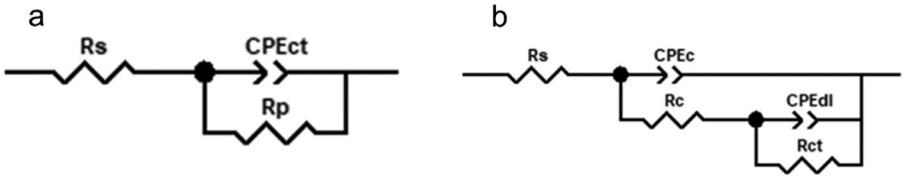

Fig. 2. The electrical circuit fitting models with one and with two time-constants applied for fitting the EIS data in (a) PBS+BSA and (b) HCl solution.

2.3. Metal release assessments

After grinding all sides to 1200 grit SiC, the specimens were ultrasonically cleaned in acetone followed by ethanol for 5 min and dried with nitrogen gas at room temperature. Finally, all specimens were stored for 24±1 h in a desiccator at room temperature (25 ± 2 °C). Triplicate specimens and a background control (blank solution without any specimen) were exposed for 4, 24 and 168 h (1 week) at 37 ± 0.1 °C in phosphate buffered saline containing 10 g/L bovine serum albumin (denoted PBS + BSA) and in 4 g/L 25% hydrochloric acid (HCl) in a dark incubator, gently bi-linearly agitated at 22 cycles/min (12° inclination). The exposed specimen area was 4.5 cm^2. Ultrapure water (resistivity 18.2 MΩ cm, Millipore, Sweden) was in all cases used as solvent. The synthetic physiological solution PBS+BSA contained 8.77 g/L NaCl, 1.28 g/L Na_2HPO_4, 1.36 g/L KH_2PO_4 (all p.a. grade, Sigma-Aldrich) and 10 g/L BSA (Sigma Aldrich A7906), with a pH adjusted to 7.2–7.4 using 50% NaOH (p.a. grade). The diluted HCl solution was used to simulate a more corrosive environment [25], such as in a crevice with lower pH and high concentrations of chlorides. After exposure, the specimens were separated from the solution and rinsed with 1 mL ultrapure water, a volume that was added to the solution samples. The specimens were then dried with nitrogen gas at room temperature and stored in a desiccator prior to further analysis (c.f. Section 2.4.). The PBS+BSA solution samples were frozen prior to digestion or digested without delay. 2 mL of the solution samples was added to 4 mL ultrapure 65% HNO_3 and 3 mL ultrapure water before digested using a microwave digester (Multiwave Go, Anton Paar, Austria) for 30 min at 180 °C until the solution was transparent and odorless. The HCl solution was diluted by ultrapure water to fit within the calibration range of the solution analysis. The dilution factors were in all cases determined by the final volume divided by the initial solution sample volume. Concentrations of iron (Fe), chromium (Cr), and nickel (Ni) in solution were determined by graphite furnace atomic absorption spectroscopy (GF-AAS, PerkinElmer Analyst 800 instrument). The limits of detection, LODs, determined from three times the average standard deviation of all blank solutions were 1.6 μg Fe/L, 0.47 μg Cr/L and 1.9 μg Ni/L for the HCl solution, and 1.1 μg Fe/L, 0.51 μg Cr/L and 1.1 μg Ni/L for PBS+BSA. Background metal concentrations were significantly lower as compared to sample concentrations and, if positive, subtracted. Released amounts of metals (μg/cm^2) were calculated by multiplying the blank-corrected concentration by the exposure volume (10 mL) and any dilution factor divided by the exposed coupon area as given in [26]. Mean values are reported with standard deviations (shown as error bars) of independent triplicate specimens. All equipment in contact with the solution samples was acid-cleaned using 10 vol.-% HNO_3 for at least 24 h and rinsed four times with ultrapure water.

2.4. X-ray photoelectron spectroscopy (XPS)

XPS measurements were performed on duplicate locations of as-received, abraded, and exposed and rinsed (with ultrapure water) specimens for surface compositional analysis of the outermost surface (approx. 5–10 nm). Wide and high-resolution spectra (pass energy 20 eV) for Fe 2p, Cr 2p, Ni 2p, Mn 2p, Cl 2p, O 1s, and C 1s were obtained using an UltraDLD spectrometer (Kratos Analytical, monochromatic 150 W, Al X-ray source on areas sized 700 × 300 μm). All binding energies were corrected to the C 1s peak at 285.0 eV. Ni was only observed in its metallic state ($2p_{3/2}$: 853.1 ± 0.3 eV), and Mn in its oxidic state ($2p_{3/2}$: 641.3 ± 0.3 eV, 643.6 ± 0.09 eV). The $2p_{3/2}$ peaks of Fe and Cr were separated into their metallic (Fe: 707.4 ± 0.4 eV, 708.3 ± 0.1 eV; Cr: 574.4 ± 0.4 eV) and oxidic (Fe: 710.6 ± 0.9 eV, 713.0 ± 0.9 eV; Cr: 576.8 ± 0.4 eV, 578.2 ± 0.4 eV) fractions to quantify their relative amounts.

2.5. Corrosion assessments

All corrosion investigations were conducted at 37 ± 0.5 °C using a Princeton Applied Research multichannel potentiostat. A three-electrode system was used, consisting of the specimens (1 cm^2 exposed area) as the working electrode, a platinum mesh as counter electrode and an Ag/AgCl saturated KCl electrode as reference electrode. The specimens were embedded in an epoxy resin with a copper wire connection on the back side to provide electrical connection. A nail lacquer (Nail Polish, Coverage, Depend O2, Nr. 033, Lot nr. 37855, Depend Cosmetic AB, Halmstad, Sweden) was used to seal all edges to prevent crevice corrosion. Prior to the investigations, all specimens were abraded using 1200 SiC grit paper (with water) followed by ultrasonic cleaning in acetone and ethanol for 5 min, drying with nitrogen gas at room temperature, and storage for 24±1 h in a desiccator at room temperature (25 ± 2 °C).

The study included open circuit potential (OCP), cyclic potentiodynamic polarization and electrochemical impedance spectroscopy (EIS) investigations in both PBS+ BSA and HCl. OCP measurements were performed for 1 h prior to the electrochemical investigations. Cyclic polarization was carried out with a scan rate of 1 mV s^{-1} scanning from −0.25 V vs. OCP to 1.2 V vs. Ag/AgCl sat. KCl or when the current reached 0.1 mA cm^{-2}, followed by a reverse scan back to the measured corrosion potential. EIS was conducted at OCP with an alternating current (AC) amplitude of 10 mV_{rms} and a frequency range from 10,000 Hz to 0.01 Hz. The EIS results of PBS+BSA were fitted using the Randles circuit, as shown in Fig. 2a. In this model, R_s and R_p reflect the solution resistance and charge-transfer resistance, respectively. A constant phase element (CPE) was used instead of a pure capacitance due to the non–homogeneous distribution of the charge at an oxide/electrolyte interface. The impedance of the CPE defined as:

$$Z_{CPE} = \left[Y_0(jw)^n\right]^{-1} \quad (1)$$

where Y_0 is the magnitude of CPE, j the imaginary unit, ω the angular frequency, and n the experience index, which is 1 for an ideal capacitance and between 0.5 and 1 for a non-ideal capacitance. An electrical equivalent circuit with two time-constants (Fig. 2b) was used to fit the EIS data in the diluted HCl solution. R_s, R_c, R_{ct}, CPE_c, and CPE_{dl} represent the electrolyte solution resistance, corrosion layer resistance, charge transfer resistance, the CPE of the corrosion layer capacitance, and the CPE of the electrical double-layer capacitance, respectively [27].

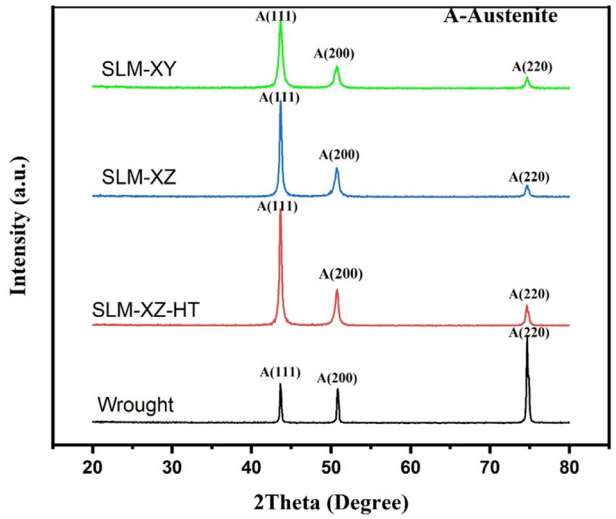

Fig. 3. XRD patterns, off-set for clarity, for wrought and SLM specimens of 316L.

2.6. Statistical evaluation

A student's *t*-test for unpaired data with unequal variance (KaleidaGraph v.4.0) was used to test whether differences between two datasets were statistically different [$p<0.05$ (the probability of equality is less than 5%)].

3. Results and discussion

3.1. Microstructural evaluations

The XRD evaluations (Fig. 3) demonstrated typical characteristic peaks of austenite for the wrought and the SLM specimens, assigned using the standard reference pattern JCPDS 31-0619 [17]. No ferrite, sigma, carbides, or other secondary phases were identified.

The microstructure and grain sizes, grain boundary angles and grain shapes were strongly depending on the fabrication type. The wrought 316L specimen showed a typical austenitic structure with equiaxed grains with a predominance of high angle grain boundaries and several twins (60⟨111⟩), Figs. 4 and S1 (supplementary information), and only few areas with visible δ-ferrite (Figs. 4 and S3), further discussed in Section 3.5. The presence of δ-ferrite seemed to correlate with the rolling direction (flattened in the x-direction, Fig. S3).

In contrast to straight line grain boundaries observed for wrought 316L, wavelike grain boundaries were seen for the SLM specimens, Fig. 4. These observations are in agreement with reported findings [11]. As evident from the phase distribution maps, no δ-ferrite was observed for any of the SLM specimens, Fig. 4. As clearly visible from the inverse pole figures (IPF), the SLM-XY and SLM-XZ specimens exhibited more low-angle grain boundaries compared with the wrought specimen. Compared with the SLM-XZ specimen, the specimen fabricated perpendicular to the SLM direction (SLM-XY) showed the highest number of low-angle grain boundaries, and a large distribution in grain sizes dominated by large grains. This is probably related to improved heat conduction (faster cooling rate) in this direction (transverse plane). The SLM specimens showed generally longer grain boundaries than the wrought counterpart. The measured average grain size decreased for the specimens in the following way: 39 μm (SLM-XY) ≥ 37 μm (SLM-XZ) > 29 μm (wrought) ≈ 28 μm (SLM-XZ-HT).

The IPF maps and grain boundary angles of the SLM-XZ-HT specimen were very similar to the non-heat-treated SLM XZ specimen, Fig. 4, which implies lack of recrystallization for the former specimen. Similar conclusions were drawn from both the LOM and the SEM images (Figs. S1, S2). EDS mapping showed uniform distributions of Fe, Cr, Ni, and Mo, Fig. S4. Also, EDS mapping of Mo in parallel of the EBSD investigations (most sensitive technique) showed uniform distribution of Mo for the SLM specimens, Fig. S5.

3.2. Release of metals

Fig. 5 shows the amount of Fe, Cr and Ni released per surface area (μg cm^{-2}) from wrought and SLM (XY, XZ and XZ-HT) 316 L specimens after 4, 24 and 168 h of exposure in solutions of PBS+BSA (Fig. 4a–c) and HCl (Fig. 5d–f). The release of metals increased for most conditions with exposure time. The trend was in all cases more evident for Cr in PBS+BSA (Fig. 5b), as the amount of released Cr was initially below the limit of detection and first detectable in solution after 24 h of exposure. In HCl, most Cr was released during the first 4 h of exposure (Fig. 5e) with only a minor increase with time. These findings are in accordance with

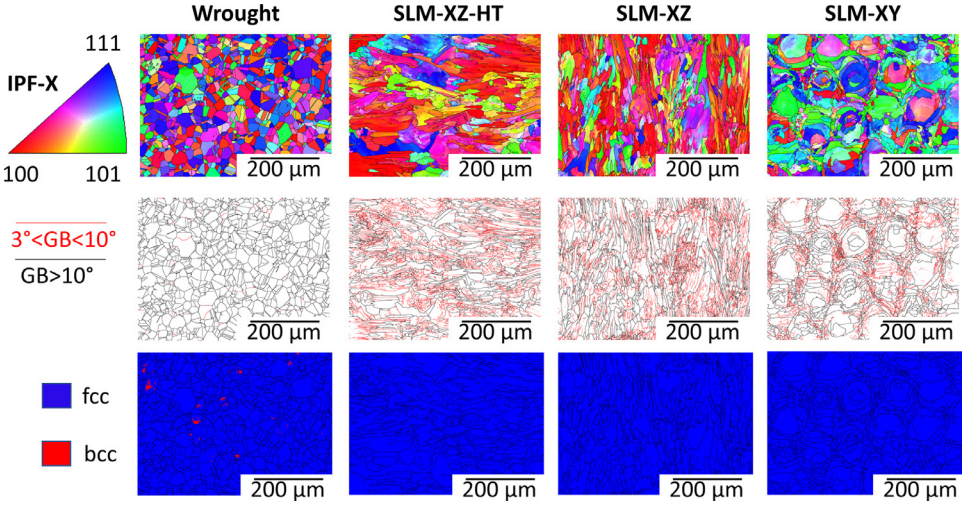

Fig. 4. Microstructures of wrought, as-printed and printed and post heat treated 316L. Top row: EBSD inverse pole figure (IPF) mapping in the x-direction showing the grain orientations for wrought, SLM-XY, SLM-XZ and SLM-XZ-HT specimens, Middle row: EBSD band contrast maps for the different specimens (red: grain boundaries, GBs, inclined between 3 and 10°, and black: GBs inclined > 10°), and Bottom row: Phase distributions (face centered cubic, fcc, austenite – blue; body centered cubic, bcc, ferrite – red). (For interpretation of the references to color in this figure legend, the reader is referred to the web version of this article.)

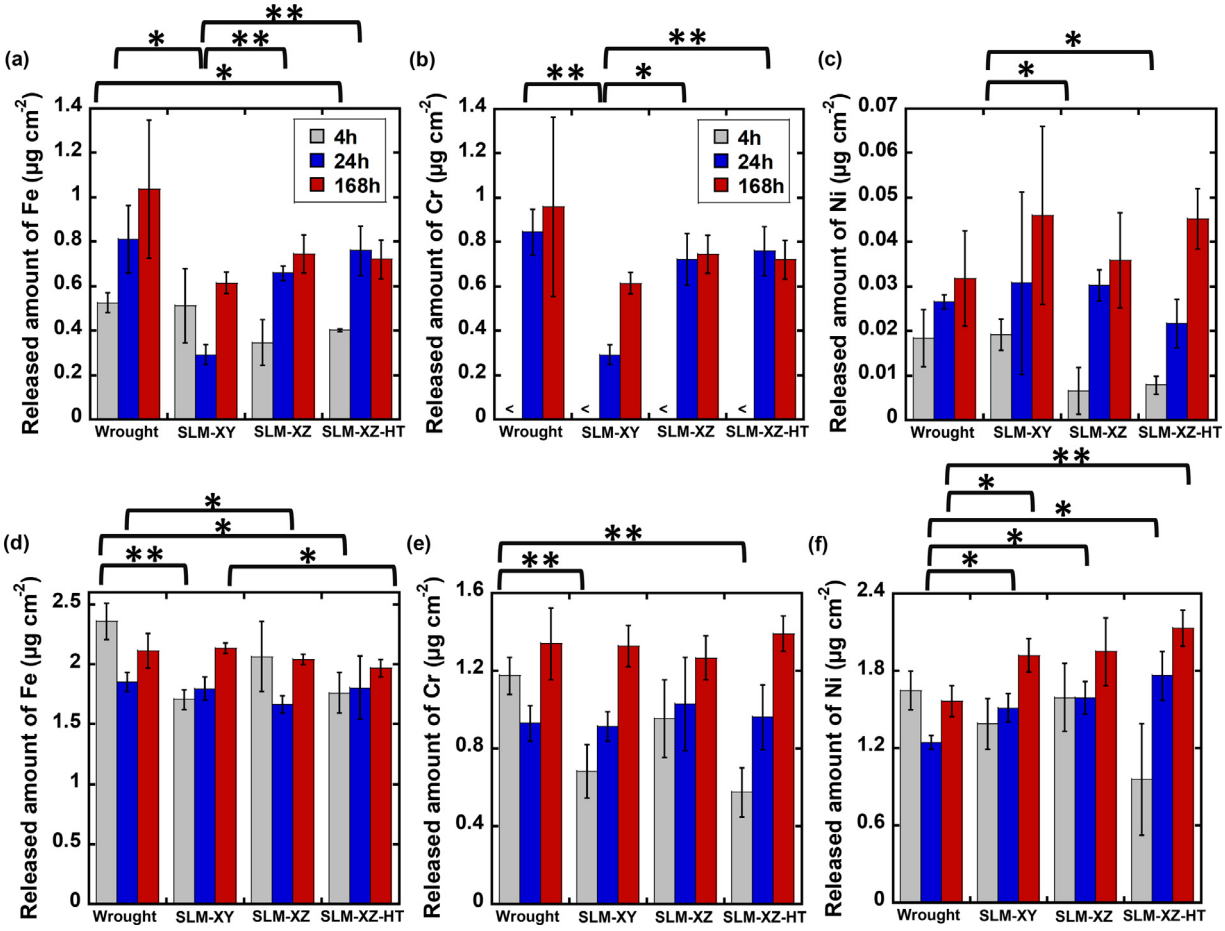

Fig. 5. Released amounts of Fe (a), Cr (b) and Ni (c) per surface area (µgcm^{-2}) from wrought and SLM (XY, XZ and XZ-HT) 316L in PBS+BSA after 4, 24 and 168 h of exposure; and corresponding findings of Fe (d), Cr (e) and Ni (f) released in diluted HCl. The error bars show the standard deviation of independent triplicate specimens. Statistical significance of differences between two types of specimens for the same exposure duration are presented, * for $p<0.05$ and ** for $p<0.01$. < - below LOD.

previous studies on the release of Cr from ferrochromium alloy powders exposed to similar conditions, even though the effect was even more pronounced compared to PBS [28]. The relatively high release of Cr in PBS+BSA after 24 and 168 h is further discussed in Section 3.5.1.

More metals (Fe, Cr and Ni) than observed for the SLM specimens were released from the wrought 316 L specimen and occurred in both solutions predominantly within the first 4 h of exposure, with observed statistical significance for Fe release in PBS+BSA and HCl ($p<0.05$), and Cr release in HCl ($p<0.01$). The SLM-XY-HT specimen displayed in most cases the lowest levels of released metals after 4 h of exposure. This is further discussed in Sections 3.4.1 and 3.5.

After one week (168 h) of exposure in either PBS+BSA or in HCl, there was no clear difference in metal release among the different specimens. Higher amounts of released Fe, Cr and Ni were observed for all specimens in HCl compared with PBS+BSA, with small differences for Cr, and higher release for both Fe (2-fold) and Ni (50-fold).

3.3. X-ray photoelectron spectroscopy (XPS)

The relative metal mass contents in the outermost surface of the different specimens are presented in Fig. 6. As-received SLM specimens revealed significant differences in their surface oxide composition as a function of their 3D-printing strategy (parallel or perpendicular to the laser) and if heat treated. The SLM-XZ specimens, printed parallel to the laser direction, showed the presence of manganese oxides (641.3 ± 0.3 eV, 643.6 ± 0.09 eV) [29] and carbides (283.3 ± 0.3 eV) [30] along with iron oxide (710.6 ± 0.9 eV, 713.0 ± 0.9 eV) and trivalent chromium oxide (576.8 ± 0.4 eV, 578.2 ± 0.4 eV) [29], while the perpendicular-aligned specimen SLM-XY only revealed oxidized iron. No metallic signals were observed for any of the as-received SLM specimens, indicative of a thickness exceeding the information depth of the XPS (5–10 nm) technique.

Once the SLM specimens were abraded, their outermost surface composition became very similar and comparable to the wrought reference. After one week of exposure in PBS+BSA, there was, in all cases, a clear evidence of adsorbed proteins observed by an increased fraction of carbon (data not shown), and statistically significantly increased signals for carbon with peaks centered at 286.3 ± 0.3 eV and 288.6 ± 0.2 eV corresponding to Cα (peptidic residues), C–O, and C–N bonds, and N–C=O bonds and/or O–C=O bonds [31], respectively. In most cases, the Cr fraction within the utmost surface oxide increased, although this was only statistically significant for the wrought and SLM-XZ specimens. After exposure to the HCl solution, all specimens revealed a significantly ($p<0.01$) increased Cr oxide fraction and a reduced oxide thickness ($p<0.05$ for wrought and SLM-XZ), as judged from a significantly increased metal to oxide ratio compared to the abraded specimens. Reductive dissolution in dilute HCl has been reported [32,33]. Chlorides (199.0 ± 0.2 eV) [34] were observed only after exposure in HCl

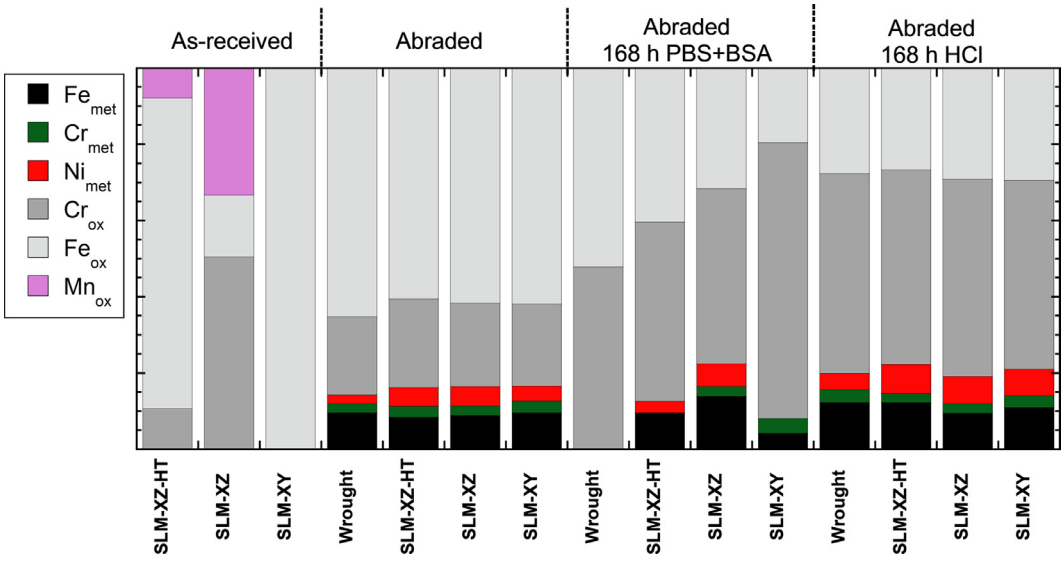

Fig. 6. Relative metal content (metallic and oxidic fractions) of Fe, Cr, Ni, and Mn in the outermost (5–10 nm) surface of as-received SLM specimens, abraded wrought 316L (for reference) and abraded SLM specimens exposed for 168 h in PBS + 10 g/L BSA or in GST at 37 °C. Corresponding XPS spectra in Fig. S6 (Supplementary material).

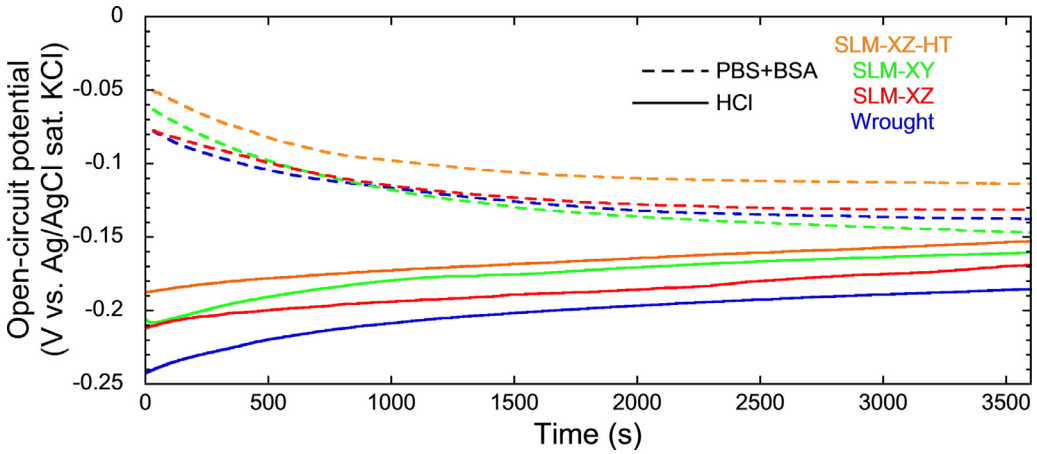

Fig. 7. Representative open-circuit potential (OCP) curves vs. time (1 h) in PBS+BSA and HCl solution at 37 °C for wrought and SLM 316L specimens.

(data not shown), most probable as residues from the exposures. In agreement with previous studies, reviewed in [35], Ni was enriched beneath the surface oxide in a higher concentration than in the bulk (10 wt%). Its presence and the reduced oxide thickness in diluted HCl combined with the possible presence of surface defects / pits could explain the higher Ni release observed in the HCl solution (Fig. 5).

3.4. Corrosion examinations

3.4.1. OCP and EIS measurements

Changes in open circuit potential (OCP) during 1 h of immersion in PBS+BSA (pH 7.3) and HCl (pH 1.5) at 37 °C are presented in Fig. 7. In PBS+BSA, the OCP decreased towards more negative potentials reaching quasi-stationary values for all specimens. This behavior is consistent with previously reported OCP measurements of 316L in PBS containing proteins related to phosphate adsorption and inhibited cathodic and/or enhanced anodic reactions upon protein adsorption [21,36–38]. The OCP was for all specimens in PBS+BSA within the stability zones (passive behavior) of Fe_2O_3, Cr_2O_3, and ternary Fe–Cr–Ni system in their equilibrium pH-potential (Pourbaix) diagrams at pH 7.3 [39,40]. In the HCl solution, in contrast, the measured OCP values coincided with the active region of Fe in the Pourbaix diagram (dissolution of iron to Fe^{2+} ions at pH = 1.5 and E=−240 to −160 $mV_{Ag/AgCl}$). The OCP values increased towards more positive values, indicative of the stabilization of the passive oxide due to the observed enrichment of chromium (c.f. Section 3.3) in the surface oxide at acidic conditions [41]. The results agree further with recent findings for SLM 316 L immersed in HCl (0.4 mol/L) at room temperature [27].

The smooth OCP curves did not indicate any metastable or active pitting corrosion, Fig. 7. The SLM specimens seemed to have a sufficiently low porosity that did not result in any pitting events at OCP during the 1 h testing period [14].While the overall trends in OCP were similar for all specimens, significant differences in OCP levels were observed between different specimens, Fig. 7.

Compared to all other specimens, the heat treated SLM specimen (SLM-XZ-HT) showed the noblest OCP in both solutions. In contrast, the wrought 316L specimen revealed clearly the lowest (most negative) OCP value in HCl.

Electrochemical impedance spectroscopy (EIS) measurements were conducted after 1 h at OCP conditions in both solutions and for all specimens. EIS is a non-destructive and sensitive method to gain information about the characteristics of the surface layer (surface oxide and any adsorbed species) and on prevailing corrosion mechanisms in a given environment [42]. The Nyquist and Bode plots acquired for both solutions are presented in Fig. 8. Negative phase angle values between 60° and 80° indicate a

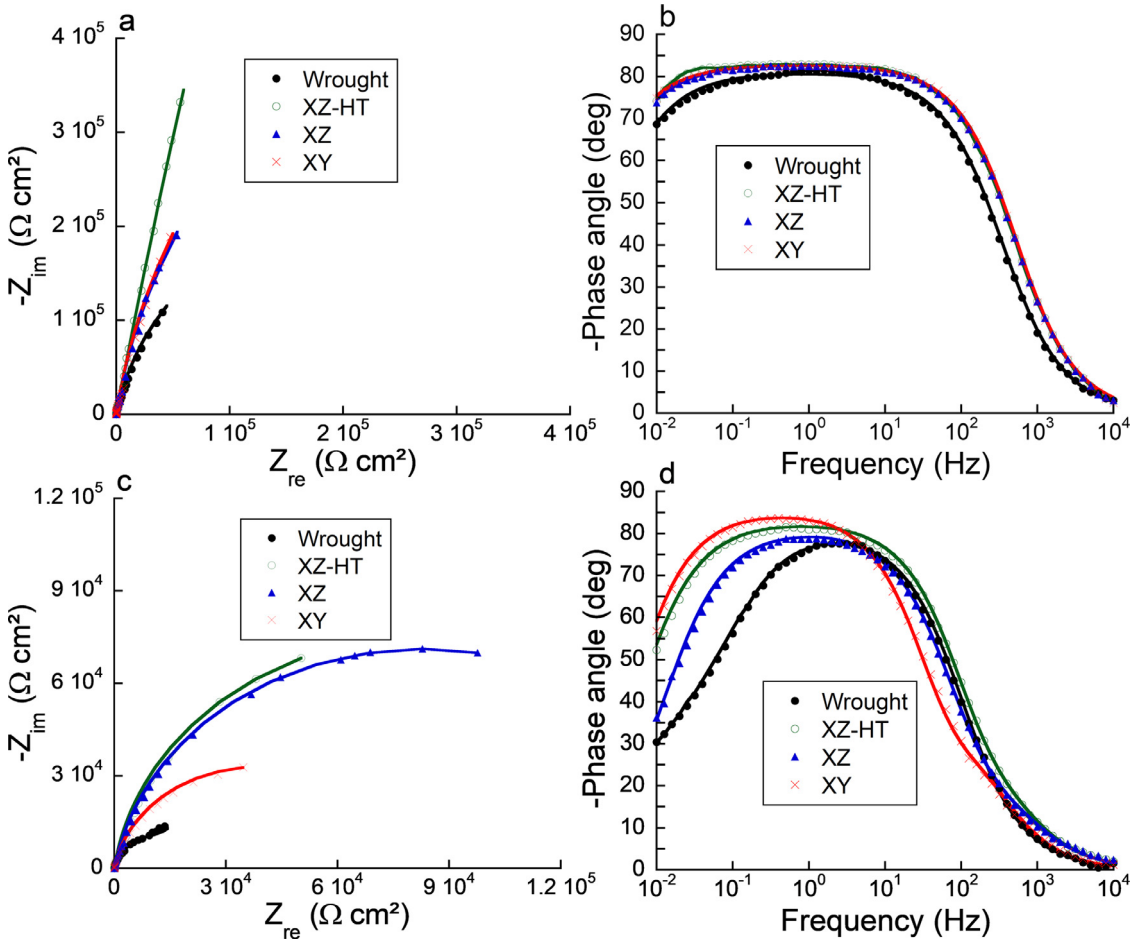

Fig. 8. Representative EIS plots acquired after 1 h immersion at 37 °C in PBS+BSA (a) Nyquist and (b) Bode plots, and in HCl solution (c) Nyquist and (d) Bode plots. The electrical circuit fitting models with one or two time-constants are presented in Fig. 2. (For interpretation of the references to colour in this figure legend, the reader is referred to the web version of this article.)

mainly capacitive surface layer. The radius of the capacitive arc in the Nyquist plots is a measure of the corrosion performance: the larger the capacitive loop, the better the corrosion resistance [36]. Consistent with the OCP measurements, the corrosion resistance was for all specimens greater in PBS+BSA compared with the HCl solution. The heat treated SLM specimen (XZ-HT) showed the best corrosion resistance in both solutions, and the wrought specimen the worst behavior in both solutions, Fig. 8. The improved corrosion resistance of SLM 316 L compared with wrought surfaces agrees well with reported findings [11].

In PBS+BSA, the Nyquist curves exhibited only one capacitive loop in the entire frequency range, indicative of the formation of a protective surface layer. The electrical circuit fitting model and the EIS fitting results in PBS+BSA are presented in Fig. 2a and Table 2. The low chi-square values ($\chi 2$) reflect a good fitting (<0.009). A similar fitting circuit has been used in other studies on SLM 316L in PBS [43] and in NaCl solutions [17,44,45]. Passivation and adsorption of albumin have also been reported to be explained by this model [36]. The adsorption of proteins and presence of chlorides likely influence the charge transfer resistance [43].

In the diluted HCl solution, an electrical equivalent circuit with two time-constants was used to fit the EIS data, Fig. 2b and Table 2. This circuit has been applied in previous studies of SLM 316L in different aggressive solutions such as HCl (0.4 mol/L) [27] and NaCl (1 M, pH 3) [46]. The fitting EIS data for the HCl solution are reported in Table 2. An excellent agreement between experimental and theoretical values of the modeling was reflected in chi-squared values ($\chi 2$) <0.005. Based on the Stern-Geary equation [27], the corrosion rate is inversely dependent on R_{ct}. CPE is indicative of the thickness of the oxidized layer [47].

The results clearly show higher corrosion resistance for all SLM specimens in both solutions, and in particular for the SLM-XZ-HT specimen, compared to the wrought specimen. This is also in agreement with literature observations [48].

3.4.2. Cyclic polarization tests

The pitting corrosion susceptibility and passive current density of the different specimens were evaluated using cyclic polarization, Fig. 9 and Table 3. A larger area of a positive hysteresis loop indicates more susceptibility to pitting corrosion [49]. The pitting potential (E_{pit}) corresponds to the potential where a slight change in potential leads to the rapid increase of the current density. A larger E_{pit} is indicative of superior pitting corrosion resistance (less pitting corrosion susceptibility). The repassivation potential (E_{rp}) is determined as the confluence point between the reverse scan and the forward scan. A more active (negative) value of E_{rp} means a lower resistance of the material to pit growth [49].

In PBS+BSA, all specimens exhibited a negative hysteresis, indicative of no pitting corrosion. These results are in agreement with literature findings [8]. Optical micrographs after 168 h in PBS+BSA at OCP indicated the absence of visible pits (Fig. S7, supplementary material). This is further discussed in Section 3.5.1.

In agreement with findings for wrought and bed fusion-laser 316L in 0.1 M HCl, all specimens showed an active-passive behavior

Table 2
Fitting data (average and standard deviation of at least three independent specimens) based on the equivalent circuit models used for PBS+ BSA and HCl solutions. Models with one time constant (Randles equivalent electrical circuit) and two time constants were applied in PBS+BSA and HCl solution, respectively.

PBS+BSA								
Sample	R_S (Ω cm^2)	CPE1 (μF cm^{-2})	n 1	R_p (kΩ cm^2)	CPE1 (μF cm^{-2})	n 2	R_{ct} (Ω cm^2)	χ^2 ($\times 10^{-3}$)
Wrought	14± 1	113 ± 10	0.91	150± 10	–	–	–	<7
SLM-XY	13 ± 2	102 ± 8	0.90	322± 15	–	–	–	<9
SLM-XZ	14± 0.5	105 ± 12	0.91	5600 ± 25	–	–	–	<2
SLM-XZ-HT	13 ± 3	100 ± 5	0.89	6800 ± 18	–	–	–	<2
HCl solution								
Sample	R_S (Ω cm^2)	CPE_c (μF cm^{-2})	n 1	R_c (Ω cm^2)	CPE_{dl} (μF cm^{-2})	n 2	R_{ct} (Ω cm^2)	χ^2 ($\times 10^{-3}$)
Wrought	18 ± 2	142 ± 8	0.85	41,800 ± 70	511 ± 35	0.91	2120 ± 85	<5
SLM-XY	20 ± 1	66 ± 10	0.9	28.0 ± 8	79 ± 11	0.9	36,200 ± 135	<1
SLM-XZ	17± 3	80 ± 13	0.9	14.5 ± 10	48 ± 16	0.9	55,100± 510	<0.5
SLM-XZ-HT	18± 2	32 ± 15	0.9	47.2 ± 5	28 ± 8	0.9	58,800 ± 230	<1

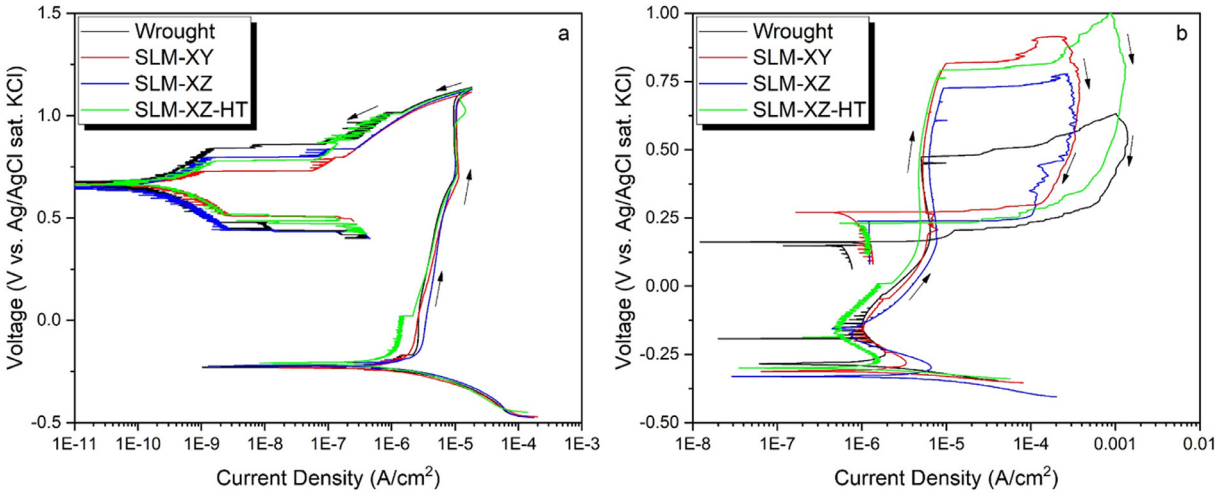

Fig. 9. Cyclic polarization curves for SLM and wrought 316L after 1 h immersion at OCP (37 °C) in (a) PBS + BSA and (b) diluted HCl.

Table 3
Corrosion potentials (E_{corr}/V), passivation current densities (i_p / μA cm^{-2}), breakdown potentials (E_{BP}/V), pitting potentials (E_{pit}/V), repassivation potentials (E_{rep}/V), and the difference between pitting and repassivation potentials (V), based on potentiodynamic polarization of at least triplicate specimens of SLM and wrought 316L after 1 h immersion at OCP in PBS+BSA and HCl solution (37 °C, scan rate:1 mV s^{-1}.).

Solution	PBS+BSA			HCl solution				
Material	E_{corr} (V)	i_p (μA•cm^{-2})	E_{BP} (V)	E_{corr} (V)	i_p (μA•cm^{-2})	E_{pit} (V)	E_{rep} (V)	(E_{pit} - E_{rep}) (V)
Wrought	−0.23±0.06	2.5 ± 0.12	1.1 ± 0.01	−0.29±0.03	2.5 ± 0.5	0.48±0.03	0.17±0.03	0.31
SLM-XY	−0.22±0.03	1.9 ± 0.05	1.1 ± 0.03	−0.31±0.01	3 ± 0.2	0.82±0.01	0.28±0.03	0.54
SLM-XZ	0.22±0.07	2.3 ± 0.08	1.1 ± 0.02	−0.33±0.02	6 ± 0.4	0.73±0.01	0.24±0.03	0.49
SLM-XZ-HT	−0.21±0.02	0.9 ± 0.03	1.1 ± 0.05	−0.30±0.03	0.9 ± 0.03	0.81±0.05	0.24±0.02	0.57

in HCl [20]. A positive hysteresis was observed during the reverse sweep for all specimens, indicative of pitting corrosion susceptibility. Pitting corrosion (pits of varying size) was also evident from optical imaging after 168 h at OCP (one week), Fig. S8 (Supplementary material). All SLM specimens showed a superior pitting corrosion resistance with fewer and smaller sized pits compared to the wrought counterpart. No measurable differences were observed between the SLM materials. An evident difference was observed in the repassivation behavior between the SLM and the wrought specimen after stable pit growth, Table 3 (E_{pit} – E_{rep}), being more difficult, with a later repassivation, for the SLM surfaces. This observation is in a good agreement with reported findings [14,50] and may be related to pores, further discussed in Section 3.5.

The passive current density of the heat-treated specimen SLM-XZ-HT was significantly lower as compared to all other specimens in both solutions, further discussed in Section 3.5.

3.5. Further discussion

3.5.1. Metal release and corrosion mechanisms

Relatively high levels of Cr were released from all specimens in PBS+BSA after 24 and 168 h of exposure. Fig. 10 compares the release of Fe, Cr, and Ni in PBS+BSA from wrought 316L in this study with a previous study on the same wrought 316L material, but with slightly different experimental conditions (mainly sampling and solution preparation prior to trace metal solution analysis). This study used a rinse-off procedure to ensure that any loosely attached proteins or metal precipitates on the surfaces were rinsed off and included in the trace metal solution analysis. The results imply that these precipitates were primarily enriched in Cr, findings supported by a recent study on metal-induced human serum albumin aggregation [51], in which the trivalent Cr ion was inducing a greater extent of protein aggregation as

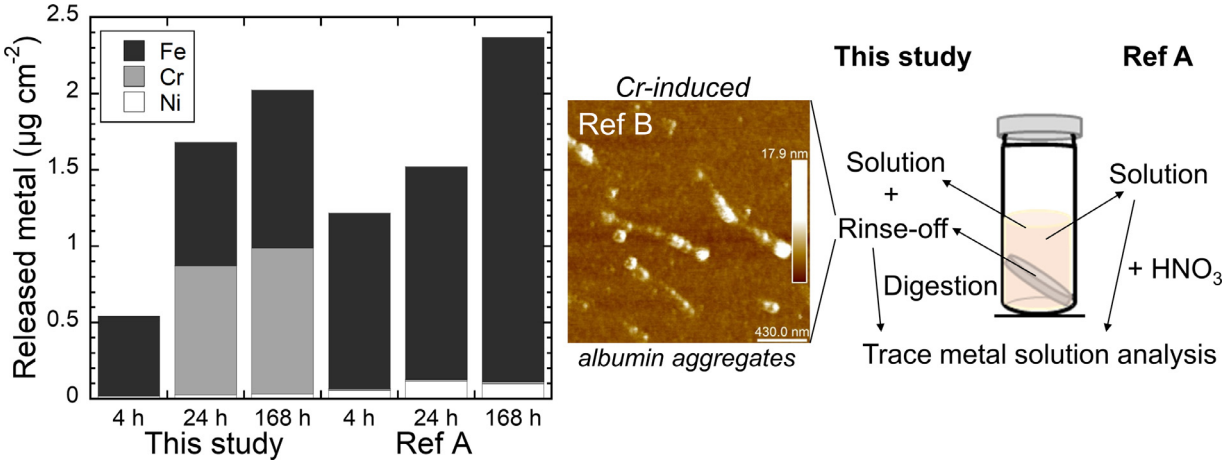

Fig. 10. Released amounts of Fe, Cr, and Ni per surface area (µg cm^{-2}) from wrought 316L in PBS+BSA after 4, 24 and 168 h of exposure in this and a previous study (ref A [83]). As illustrated in the figure, the main differences between this study and ref A were related to the sampling and solution preparation. The rinse-off procedure applied in this study could also enable the collection of precipitated Cr-induced albumin aggregates. The presence of such precipitated aggregates has earlier been identified (ref B) by means of atomic force microscopy [51].

compared to divalent Ni and cobalt (Co) ions. Rapid precipitation was evident for the Cr-induced albumin aggregates in that study [51]. This suggests that the rinse-off procedure applied in this study was vital to avoid any underestimation of released Cr in albumin-rich solutions. A delayed release of metals in PBS+BSA, in particularly of Cr, Fig. 10, is probably related to the adsorption and surface interactions with proteins. Adsorption of proteins has been shown to result in a delayed metal release mechanism due to slow kinetics in protein-metal conjugate detachment [22,23]. There was no indication of any metastable pitting events or active corrosion at OCP for any specimens in PBS+BSA, which means that the metal release process mostly was driven by surface reactions. We speculate that the presence of the albumin proteins inhibits the susceptibility to pitting corrosion. This hypothesis is based on *i*) literature findings showing that SLM 316L and wrought 316L are susceptible to pitting corrosion at oxidative potentials in PBS and similar solutions without proteins [43,52], and *ii*) comparative studies that report enhanced pitting corrosion resistance in the presence of albumin and whey proteins (containing albumin) [26]. This could be explained by the adsorption of proteins and the electrostatic repulsion between the net-negatively charged albumin at pH 7.4 [53] and chlorides.

Relatively high amounts of Ni were released in the HCl solution. HCl-surface reactions resulted in a thinning of the surface oxide [32,33], c.f. Section 3.3. Furthermore, pit formation was evidently taking place in the HCl solution, observed after 1 week of exposure at OCP. Since Ni is enriched beneath the surface oxide [54,55], also indicated by the XPS findings in this study, pitting corrosion reactions could explain the observed increased amounts of released Ni in diluted HCl. In the diluted HCl solution, almost all metals were released during the first 4 h of exposure, indicating a rapidly passivating oxide. This observation correlated with a strong Cr enrichment in the outermost surface observed by XPS.

After one week of exposure and for both investigated solutions, the amounts of released metals were relatively similar among the different specimens. The accelerated and short-term corrosion tests correlated best with the metal release results after 4 h showing similar differences among the specimens. Similar amounts of released metals for the different specimens were found after longer exposure periods. Differences in pitting corrosion susceptibilities, which were investigated in the cyclic polarization tests, were hence found to not be the predominating explanations for the total amounts of released metals after one week of immersion at open circuit potential in diluted HCl.

3.5.2. Effect of cooling rate, grain refinement, and δ-ferrite

The presence of δ-ferrite in the wrought specimen (Fig. 4) could be a factor that reduces its pitting resistance [56]. The extent of residual δ-ferrite in 316L strongly depends on cooling rates and the time of possible transformation to austenite [57], e.g. during heating of successive layers. It is hence strongly influenced by the AM process parameters, technique, and power [8,58-61]. The high cooling rates taking place during the SLM process (~10^7 K/s) [62,63] mean that a ferritic structure could be expected for 316L [64]. We hence speculate that the heating from subsequent layers is sufficient to transform any residual ferritic structures to austenite. Such effects have been observed for a SLM CoCrMo alloy, with a metastable phase (only fcc γ phase) at the outermost surface and a transformed phase (both γ and hexagonal ε phases) throughout the bulk material (for polished specimens) [65]. The observation of an entirely austenitic structure of the abraded SLM 316L specimens in this study is consistent with literature findings [11,66,67].

Compared with wrought 316L, the high cooling rates associated with the SLM process lead to the formation of substantially finer sub-grain cellular/columnar microstructure, which have been shown to improve the corrosion resistance [68]. Depending on exposure conditions, the corrosion resistance can either be improved by the microstructure due to increased passivity or worsened due to high grain boundary density at conditions when grain boundaries are preferential sites for corrosion [69]. Enhanced pitting corrosion potentials and lower corrosion current densities of the SLM 316L specimens compared to the wrought 316L are in general agreement with the literature [11,17,27,70–73], even though conflicting results are reported [20,50,63]. We speculate that the absence of precipitates and Cr depletion at grain boundaries, as well as the absence of MnS inclusions [63,70], for all SLM specimens in this study have been the main reasons why the surface density of grain boundaries of the abraded specimens was not an important factor for the corrosion resistance and metal release. Hence, no differences in terms of corrosion and metal release were observed for the abraded SLM-XZ and SLM-XY specimens.

3.5.3. Effect of inclusions and heat treatment

The density, size and shape of inclusions like MnS are important factors for the pitting corrosion resistance of stainless steels [74–76] and the metal release mechanism in the presence of proteins [21]. It has been demonstrated that the formation of MnS (typically micrometer-sized) and associated chromium-depleted zones are avoided for SLM 316L surfaces [70]. This has also been shown

in this study. Although the extent of micrometer-sized MnS inclusions of the wrought 316L was low compared to other wrought stainless steel grades [21], the sizes of its concomitant pits were after one week of immersion in diluted HCl at OCP larger compared to the SLM 316L specimens. The size of MnS inclusions is crucial for the probability of pitting corrosion [76]. The formation of nano-inclusions due to the accumulation of O, Al, Si and Mn have been observed for SLM 316L [63]. This is most probably related to the high oxygen affinity of Al, Si, and Mn, and known for other rapid solidification processes of 316L [77,78]. It is also in good agreement with the Mn-enriched surface oxide for the as-printed SLM surfaces of this study. Other defects, such as solute segregation, melt-pool boundaries and grain boundaries, need to be considered for pitting corrosion of SLM specimens [79]. In this context, heat treatment can be an important tool [79], since this treatment could reduce the number of other defects and relax residual stresses in SLM specimens [80]. According to the results of this study, the post heat treatment at 900 °C improved the corrosion resistance of SLM 316L, without affecting the microstructure and elemental distribution significantly. This finding is in agreement with other studies showing post heat treatments of SLM specimens to relax internal stresses and to homogenize their composition [63,81]. In this study, the SLM-XZ-HT specimen showed superior pitting corrosion resistance. This is in contrast with literature findings [63] that report reduced pitting corrosion resistance of heat treated SLM 316L (at 1050 and 1200 °C for 0.5, 1 and 2 h in argon followed by water cooling) in 3.5 wt% NaCl, attributed to the formation of weak passive films and enlarged pores after the heat treatment.

3.5.4. Effect of porosity

In this study, the SLM specimens were fabricated with the highest density possible and exhibited a very high pitting corrosion resistance at all conditions. Porosity has been reported crucial especially for pitting corrosion of SLM 316L or comparable specimens [16,58,63,70,74,82]. Nevertheless, small differences in pitting potentials have been reported for SLM 316L specimens of different porosity [14]. The overall conclusion is hence a lack of relationship between the pitting potential and the porosity [74]. However, as observed in this study and in previous studies [13,50], the presence of pores could deteriorate the ability of the material to repassivate.

3.5.5. Need for future studies

Future studies on SLM materials should include mechanistic studies on both metal release and corrosion in simulated physiological environments containing proteins and some worst-case corrosive factors such as high acidity, high amounts of chlorides and/or high redox potential as such conditions could be relevant in e.g. crevices, conditions of inflammation, or infection.

4. Conclusions

1. All SLM specimens revealed an austenitic microstructure without any amounts of δ-ferrite as observed for wrought 316L. The surface oxide composition of as-printed SLM specimens was strongly dependent on the building direction and the post heat treatment. After abrasion, no difference in surface composition was discerned, either among the SLM specimens or compared with the wrought 316L specimen. The heat treatment of the SLM specimens had a minor effect on the microstructure and elemental distribution.
2. Significantly more Ni was released in diluted HCl compared to PBS+BSA as a result of a reduction of the surface oxide thickness and possibly pitting corrosion. The SLM specimens showed, in contrast to the wrought specimen, a lower susceptibility for pitting corrosion in HCl. Still, the release of Ni was similar after one week at OCP for the SLM and the wrought 316L specimens. A strong enrichment of Cr in the surface oxide was coupled to a strongly reduced metal release rate with time.
3. Relatively high amounts of Cr were released in PBS+BSA after one day and one week of exposure, most probably attributed to Cr-protein interactions. Cr was also enriched in the surface oxide. No pitting was observed for any of the specimens in PBS+BSA, most probably related to the barrier effect of adsorbed proteins repelling similarly charged chlorides from the surface.
4. The heat-treated SLM 316L specimen (XZ-HT) showed the highest charge transfer resistance, the lowest passive current density, slightly lower metal release after 4 h of exposure, and the highest OCP value among all specimens (SLM and wrought 316L).
5. No effects of SLM building direction were observed for abraded specimens from either a metal release or corrosion perspective.

Author contributions

Masoud Atapour: conceptualization, investigation, validation, formal analysis, methodology, writing – original draft, visualization, funding acquisition; Xuying Wang: investigation, formal analysis, writing – original draft, visualization; Kim Färnlund: resources, writing – review & editing; Inger Odnevall Wallinder: conceptualization, investigation, writing – review & editing, funding acquisition; Yolanda Hedberg: conceptualization, formal analysis, methodology, project administration, visualization, writing – review & editing, funding acquisition.

Funding

This work was supported by the Swedish Research Council [grant number 2015-04177]; the Swedish Governmental Agency for Innovation Systems Vinnova [2018-03,336] and involved companies; and KTH faculty grants.

Declaration of Competing Interest

None.

Acknowledgments

Amexci AB is highly acknowledged for providing the SLM specimens and Oskar Karlsson, Swerim AB, for the EBSD measurements and related discussions.

Supplementary materials

Supplementary material associated with this article can be found, in the online version, at doi:10.1016/j.electacta.2020.136748.

References

[1] M. Kaur, K. Singh, Review on titanium and titanium based alloys as biomaterials for orthopaedic applications, Mater. Sci. Eng. C 102 (2019) 844–862.
[2] R. Gorejová, L. Haverová, R. Oriňaková, A. Oriňak, M. Oriňak, Recent advancements in Fe-based biodegradable materials for bone repair, J. Mater. Sci. 54 (2019) 1913–1947.
[3] R. Barreiro-Iglesias, C. Alvarez-Lorenzo, A. Concheiro, Microalorimetric evidence and rheological consequences of the salt effect on carbopol-surfactant interactions, Progr. Colloid Polym. Sci. 122 (2003) 95–102.
[4] J. Wilson, Metallic biomaterials: state of the art and new challenges, in: B. Preetha, M.S. Sreekala, T. Sabu (Eds.), Fundamental Biomaterials: Metals, Elsevier, Duxford, UK, 2018, pp. 1–33.
[5] E.D. Herderick, Progress in additive manufacturing, J. Miner. Met. Mater. Soc. 67 (2015) 580–581.
[6] L. Chen, Y. He, Y. Yang, S. Niu, H. Ren, The research status and development trend of additive manufacturing technology, Int. J. Adv. Manuf. Technol. 89 (2017) 3651–3660.

[7] A.T. Sutton, C.S. Kriewall, S. Karnati, M.C. Leu, J.W. Newkirk, Characterization of AISI 304L stainless steel powder recycled in the laser powder-bed fusion process, Addit. Manuf. 32 (2020) 100981.
[8] D. Kong, X. Ni, C. Dong, X. Lei, L. Zhang, C. Man, J. Yao, X. Cheng, X. Li, Bio–functional and anti-corrosive 3D printing 316L stainless steel fabricated by selective laser melting, Mater. Des. 152 (2018) 88–101.
[9] E. Avcu, F.E. Baştan, H.Z. Abdullah, M.A.U. Rehman, Y.Y. Avcu, A.R. Boccaccini, Electrophoretic deposition of chitosan-based composite coatings for biomedical applications: a review, Progr. Mater. Sci. 103 (2019) 69–108.
[10] L.-.Y. Li, L.-.Y. Cui, R.-.C. Zeng, S.-.Q. Li, X.-.B. Chen, Y. Zheng, M.B. Kannan, Advances in functionalized polymer coatings on biodegradable magnesium alloys – a review, Acta Biomater. 79 (2018) 23–36.
[11] C. Man, C. Dong, T. Liu, D. Kong, D. Wang, X. Li, The enhancement of microstructure on the passive and pitting behaviors of selective laser melting 316L SS in simulated body fluid, Appl. Surf. Sci. 467-468 (2019) 193–205.
[12] J.T. Miller, H.J. Martin, E. Cudjoe, Comparison of the effects of a sulfuric acid environment on traditionally manufactured and additive manufactured stainless steel 316L alloy, Addit. Manuf. 23 (2018) 272–286.
[13] G. Sander, J. Tan, P. Balan, O. Gharbi, D.R. Feenstra, L. Singer, S. Thomas, R.G. Kelly, J.R. Scully, N. Birbilis, Corrosion of additively manufactured alloys: a review, Corrosion 74 (2018) 1318–1350.
[14] G. Sander, S. Thomas, V. Cruz, M. Jurg, N. Birbilis, X. Gao, M. Brameld, C. Hutchinson, On the corrosion and metastable pitting characteristics of 316L stainless steel produced by selective laser melting, J. Electrochem. Soc. 164 (2017) C250–C257.
[15] P. Bajaj, A. Hariharan, A. Kini, P. Kürnsteiner, D. Raabe, E.A. Jägle, Steels in additive manufacturing: a review of their microstructure and properties, Mater. Sci. Eng. A 772 (2020) 138633.
[16] F. Andreatta, A. Lanzutti, E. Vaglio, G. Totis, M. Sortino, L. Fedrizzi, Corrosion behaviour of 316L stainless steel manufactured by selective laser melting, Mater. Corros. 70 (2019) 1633–1645.
[17] M.J.K. Lodhi, K.M. Deen, W. Haider, Corrosion behavior of additively manufactured 316L stainless steel in acidic media, Materialia 2 (2018) 111–121.
[18] X. Ni, D. Kong, Y. Wen, L. Zhang, W. Wu, B. He, L. Lu, D. Zhu, Anisotropy in mechanical properties and corrosion resistance of 316L stainless steel fabricated by selective laser melting, Int. J. Miner. Metal. Mater. 26 (2019) 319–328.
[19] R.F. Schaller, A. Mishra, J.M. Rodelas, J.M. Taylor, E.J. Schindelholz, The role of microstructure and surface finish on the corrosion of selective laser melted 304L, J. Electrochem. Soc. 165 (2018) C234–C242.
[20] J.R. Trelewicz, G.P. Halada, O.K. Donaldson, G. Manogharan, Microstructure and corrosion resistance of laser additively manufactured 316L stainless steel, J. Miner. Met. Mater. Soc. 68 (2016) 850–859.
[21] Y. Hedberg, M.-.E. Karlsson, Z. Wei, M. Žnidaršič, I.O. Wallinder, J. Hedberg, Interaction of albumin and fibrinogen with stainless steel: influence of sequential exposure and protein aggregation on metal release and corrosion resistance, Corrosion 73 (2017) 1423–1436.
[22] Y. Hedberg, M.-.E. Karlsson, E. Blomberg, I. Odnevall Wallinder, J. Hedberg, Correlation between surface physicochemical properties and the release of iron from stainless steel AISI 304 in biological media, Colloid. Surf. B 122 (2014) 216–222.
[23] Y.S. Hedberg, Role of proteins in the degradation of relatively inert alloys in the human body, NPJ Mater. Degrad. 2 (2018) 26.
[24] J.R. Davis, Stainless Steels, ASM International, Materials Park, OH, 1994.
[25] M. Atapour, A.L. Pilchak, G.S. Frankel, J.C. Williams, Corrosion behavior of β titanium alloys for biomedical applications, Mater. Sci. Eng. C 31 (2011) 885–891.
[26] M. Atapour, Z. Wei, H. Chaudhary, C. Lendel, I. Odnevall Wallinder, Y. Hedberg, Metal release from stainless steel 316L in whey protein- and simulated milk solutions under static and stirring conditions, Food Control 101 (2019) 163–172.
[27] L. Chen, B. Richter, X. Zhang, X. Ren, F.E. Pfefferkorn, Modification of surface characteristics and electrochemical corrosion behavior of laser powder bed fused stainless-steel 316L after laser polishing, Addit. Manuf. 32 (2020) 101013.
[28] K. Midander, A. de Frutos, Y. Hedberg, G. Darrie, I. Odnevall Wallinder, Bioaccessibility studies of ferro-chromium alloy particles for a simulated inhalation scenario: a comparative study with the pure metals and stainless steel, Integr. Env. Asses. 6 (2010) 441–455.
[29] M.C. Biesinger, B.P. Payne, A.P. Grosvenor, L.W.M. Lau, A.R. Gerson, R.S.C. Smart, Resolving surface chemical states in XPS analysis of first row transition metals, oxides and hydroxides: cr, Mn, Fe, Co and Ni, Appl. Surf. Sci. 257 (2011) 2717–2730.
[30] J. Kovač, P. Panjan, A. Zalar, XPS analysis of WxCy thin films prepared by sputter deposition, Vacuum 82 (2007) 150–153.
[31] B. Wu, C. Mu, G. Zhang, W. Lin, Effects of Cr3+ on the structure of collagen fiber, Langmuir 25 (2009) 11905–11910.
[32] Y. Li, R. Hu, J. Wang, Y. Huang, C.-J. Lin, Corrosion initiation of stainless steel in HCl solution studied using electrochemical noise and in-situ atomic force microscope, Electrochim. Acta 54 (2009) 7134–7140.
[33] K. Sugimoto, Corrosion protection function and breakdown mechanism of passive films on stainless steels, in: Y. Waseda, S. Suzuki (Eds.), Characterization of Corrosion Products on Steel Surfaces, Springer, Berlin, Germany, 2006, pp. 1–17.
[34] M.C. Biesinger, X-ray Photoelectron Spectroscopy (XPS) Reference Pages, http://www.xpsfitting.com/search/label/Chlorine, 2020, accessed 2020-06-22.
[35] Y.S. Hedberg, I. Odnevall Wallinder, Metal release from stainless steel in biological environments: a review, Biointerphases 11 (2016) 018901-01-018901-17.
[36] D. de Castro Girão, M. Béreš, A.L. Jardini, R.M. Filho, C.C. Silva, A. de Siervo, H.F. Gomes de Abreu, W.S. Araújo, An assessment of biomedical CoCrMo alloy fabricated by direct metal laser sintering technique for implant applications, Mater. Sci. Eng. C 107 (2020) 110305.
[37] S. Karimi, T. Nickchi, A. Alfantazi, Effects of bovine serum albumin on the corrosion behaviour of AISI 316L, Co–28Cr–6Mo, and Ti–6Al–4V alloys in phosphate buffered saline solutions, Corros. Sci. 53 (2011) 3262–3272.
[38] C. Valero Vidal, A. Igual Muñoz, Study of the adsorption process of bovine serum albumin on passivated surfaces of CoCrMo biomedical alloy, Electrochim. Acta 55 (2010) 8445–8452.
[39] M. Pourbaix, Atlas of Electrochemical Equilibria in Aqueous Solutions, National Association of Corrosion Engineers (NACE), Houston, TX, 1966.
[40] B. Beverskog, I. Puigdomenech, Pourbaix diagrams for the ternary system of iron-chromium-nickel, Corrosion 55 (1999) 1077–1087.
[41] N. Mazinanian, G. Herting, I.O. Wallinder, Y. Hedberg, Metal release and corrosion resistance of different stainless steel grades in simulated food contact, Corrosion 72 (2016) 775–790.
[42] S. Mohd Yusuf, M. Nie, Y. Chen, S. Yang, N. Gao, Microstructure and corrosion performance of 316L stainless steel fabricated by Selective Laser Melting and processed through high-pressure torsion, J. Alloy Compd. 763 (2018) 360–375.
[43] M.J.K. Lodhi, K.M. Deen, M.C. Greenlee-Wacker, W. Haider, Additively manufactured 316L stainless steel with improved corrosion resistance and biological response for biomedical applications, Addit. Manuf. 27 (2019) 8–19.
[44] R.I. Revilla, B. Wouters, F. Andreatta, A. Lanzutti, L. Fedrizzi, I. De Graeve, EIS comparative study and critical Equivalent Electrical Circuit (EEC) analysis of the native oxide layer of additive manufactured and wrought 316L stainless steel, Corros. Sci. 168 (2020) 108480.
[45] Y. Zhang, B. Song, J. Ming, Q. Yan, M. Wang, C. Cai, C. Zhang, Y. Shi, Corrosion mechanism of amorphous alloy strengthened stainless steel composite fabricated by selective laser melting, Corros. Sci. 163 (2020) 108241.
[46] Z. Duan, C. Man, C. Dong, Z. Cui, D. Kong, L. wang, X. Wang, Pitting behavior of SLM 316L stainless steel exposed to chloride environments with different aggressiveness: pitting mechanism induced by gas pores, Corros. Sci. 167 (2020) 108520.
[47] M. Cao, L. Liu, Z. Yu, L. Fan, Y. Li, F. Wang, Electrochemical corrosion behavior of 2A02 Al alloy under an accelerated simulation marine atmospheric environment, J. Mater. Sci. Technol. 35 (2019) 651–659.
[48] R. Singh, M. Martin, N. Dahotre, Influence of laser surface modification on corrosion behavior of stainless steel 316L and Ti–6Al–4V in simulated biofluid, Surface Eng. 21 (2005) 297–306.
[49] M. Atapour, H. Sarlak, M. Esmailzadeh, Pitting corrosion susceptibility of friction stir welded lean duplex stainless steel joints, Int. J. Adv. Manuf. Technol. 83 (2016) 721–728.
[50] Y. Sun, A. Moroz, K. Alrbaey, Sliding wear characteristics and corrosion behaviour of selective laser melted 316L stainless steel, J. Mater. Eng. Perform. 23 (2014) 518–526.
[51] Y.S. Hedberg, I. Dobryden, H. Chaudhary, Z. Wei, P.M. Claesson, C. Lendel, Synergistic effects of metal-induced aggregation of human serum albumin, Colloid Surf. B 173 (2019) 751–758.
[52] D. Kong, C. Dong, X. Ni, L. Zhang, H. Luo, R. Li, L. Wang, C. Man, X. Li, The passivity of selective laser melted 316L stainless steel, Appl. Surf. Sci. 504 (2020) 144495.
[53] T. Peters, Serum albumin, in: C.B. Anfinsen, J.T. Edsall, F.M. Richards (Eds.), Advances in Protein Chemistry, Academic Press, 1985, pp. 161–245.
[54] I. Olefjord, L. Wegrelius, Surface analysis of passive state, Corros. Sci. 31 (1990) 89–98.
[55] T. Hanawa, S. Hiromoto, A. Yamamoto, D. Kuroda, K. Asami, XPS characterization of the surface oxide film of 316L stainless steel samples that were located in quasi-biological environments, Mater. Trans. JIM 43 (2002) 3088–3092.
[56] G.R. Mirshekari, E. Tavakoli, M. Atapour, B. Sadeghian, Microstructure and corrosion behavior of multipass gas tungsten arc welded 304L stainless steel, Mater. Des. 55 (2014) 905–911.
[57] J.W. Elmer, S.M. Allen, T.W. Eagar, Microstructural development during solidification of stainless steel alloys, Metall. Trans. A 20 (1989) 2117–2131.
[58] M.A. Melia, H.-D.A. Nguyen, J.M. Rodelas, E.J. Schindelholz, Corrosion properties of 304L stainless steel made by directed energy deposition additive manufacturing, Corros. Sci. 152 (2019) 20–30.
[59] O.O. Salman, C. Gammer, A.K. Chaubey, J. Eckert, S. Scudino, Effect of heat treatment on microstructure and mechanical properties of 316L steel synthesized by selective laser melting, Mater. Sci. Eng. A 748 (2019) 205–212.
[60] X. Xu, G. Mi, Y. Luo, P. Jiang, X. Shao, C. Wang, microstructures Morphologies, and mechanical properties of samples produced using laser metal deposition with 316L stainless steel wire, Opt. Laser Eng. 94 (2017) 1–11.
[61] M. Ziętala, T. Durejko, M. Polański, I. Kunce, T. Płociński, W. Zieliński, M. Łazińska, W. Stępniowski, T. Czujko, K.J. Kurzydłowski, Z. Bojar, The microstructure, mechanical properties and corrosion resistance of 316L stainless steel fabricated using laser engineered net shaping, Mater. Sci. Eng. A 677 (2016) 1–10.
[62] S. Gorsse, C. Hutchinson, M. Gouné, R. Banerjee, Additive manufacturing of metals: a brief review of the characteristic microstructures and properties of steels, Ti-6Al-4V and high-entropy alloys, Sci. Technol. Adv. Mater. 18 (2017) 584–610.

[63] D. Kong, X. Ni, C. Dong, L. Zhang, C. Man, J. Yao, K. Xiao, X. Li, Heat treatment effect on the microstructure and corrosion behavior of 316L stainless steel fabricated by selective laser melting for proton exchange membrane fuel cells, Electrochim. Acta 276 (2018) 293–303.
[64] Y. Hedberg, O. Karlsson, P. Szakalos, I.O. Wallinder, Ultrafine 316L stainless steel particles with frozen-in magnetic structures characterized by means of electron backscattered diffraction, Mater. Lett. 65 (2011) 2089–2092.
[65] Y.S. Hedberg, B. Qian, Z. Shen, S. Virtanen, I. Odnevall Wallinder, In vitro biocompatibility of CoCrMo dental alloys fabricated by selective laser melting, Dent. Mater. 30 (2014) 525–534.
[66] S. Krishnan, J. Dumbre, S. Bhatt, E.T. Akinlabi, R. Ramalingam, Effect of crystallographic orientation on the pitting corrosion resistance of laser surface melted AISI 304L austenitic stainless steel, Int. J. Mech. Aerosp. Ind. Mechatron. Eng. 7 (2013) 239–242.
[67] J. Lei, J. Xie, S. Zhou, H. Song, X. Song, X. Zhou, Comparative study on microstructure and corrosion performance of 316 stainless steel prepared by laser melting deposition with ring-shaped beam and Gaussian beam, Opt. Laser Technol. 111 (2019) 271–283.
[68] J. Suryawanshi, T. Baskaran, O. Prakash, S.B. Arya, U. Ramamurty, On the corrosion resistance of some selective laser melted alloys, Materialia 3 (2018) 153–161.
[69] K.D. Ralston, N. Birbilis, Effect of grain size on corrosion: a review, Corrosion 66 (2010) 075005-075005-13.
[70] Q. Chao, V. Cruz, S. Thomas, N. Birbilis, P. Collins, A. Taylor, P.D. Hodgson, D. Fabijanic, On the enhanced corrosion resistance of a selective laser melted austenitic stainless steel, Scr. Mater. 141 (2017) 94–98.
[71] M. Laleh, A.E. Hughes, W. Xu, I. Gibson, M.Y. Tan, Unexpected erosion-corrosion behaviour of 316L stainless steel produced by selective laser melting, Corros. Sci. 155 (2019) 67–74.
[72] M. Kazemipour, M. Mohammadi, E. Mfoumou, A.M. Nasiri, Microstructure and corrosion characteristics of selective laser-melted 316L stainless steel: the impact of process-induced porosities, J. Miner. Met. Mater. Soc. 71 (2019) 3230–3240.
[73] X. Ni, D. Kong, W. Wu, L. Zhang, C. Dong, B. He, L. Lu, K. Wu, D. Zhu, Corrosion behavior of 316L stainless steel fabricated by selective laser melting under different scanning speeds, J. Mater. Eng. Perform. 27 (2018) 3667–3677.
[74] M. Laleh, A.E. Hughes, S. Yang, J. Li, W. Xu, I. Gibson, M.Y. Tan, Two and three-dimensional characterisation of localised corrosion affected by lack-of-fusion pores in 316L stainless steel produced by selective laser melting, Corros. Sci. 165 (2019) 108394.
[75] J. Stewart, D.E. Williams, The initiation of pitting corrosion on austenitic stainless steel: on the role and importance of sulphide inclusions, Corros. Sci. 33 (1992) 457–474.
[76] T. Suter, T. Peter, H. Böhni, Microelectrochemical investigations of MnS inclusions, Mater. Sci. Forum 192-194 (1995) 25–40.
[77] Y. Hedberg, N. Mazinanian, I. Odnevall Wallinder, Metal release from stainless steel powders and massive sheets–comparison and implication for risk assessment of alloys, Env. Sci. Process. Impact. 15 (2013) 381–392.
[78] Y. Hedberg, M. Norell, J. Hedberg, P. Szakálos, P. Linhardt, I. Odnevall Wallinder, Surface characterisation of fine inert gas and water atomised stainless steel 316L powders: formation of thermodynamically unstable surface oxide phases, Powder Metall. 56 (2013) 158–163.
[79] C. Zhou, S. Hu, Q. Shi, H. Tao, Y. Song, J. Zheng, P. Xu, L. Zhang, Improvement of corrosion resistance of SS316L manufactured by selective laser melting through subcritical annealing, Corros. Sci. 164 (2020) 108353.
[80] P. Mercelis, J.P. Kruth, Residual stresses in selective laser sintering and selective laser melting, Rapid Prototyping J. 12 (2006) 254–265.
[81] M. Montero Sistiaga, S. Nardone, C. Hautfenne, J. Van Humbeeck, Effect of heat treatment of 316L stainless steel produced by selective laser melting (SLM), in: Proceedings of the 27th Annual International Solid Freeform Fabrication Symposium-An Additive Manufacturing Conference, 2016, pp. 558–565.
[82] D.A. Macatangay, S. Thomas, N. Birbilis, R.G. Kelly, Unexpected interface corrosion and sensitization susceptibility in additively manufactured austenitic stainless steel, Corrosion 74 (2018) 153–157.
[83] Y. Hedberg, X. Wang, J. Hedberg, M. Lundin, E. Blomberg, I. Odnevall Wallinder, Surface-protein interactions on different stainless steel grades: effects of protein adsorption, surface changes and metal release, J. Mater. Sci.: Mater. Med. 24 (2013) 1015–1033.